

Do Neural Optimal Transport Solvers Work? A Continuous Wasserstein-2 Benchmark

Alexander Korotin

Skolkovo Institute of Science and Technology
Moscow, Russia
a.korotin@skoltech.ru

Lingxiao Li

Massachusetts Institute of Technology
Cambridge, Massachusetts, USA
lingxiao@mit.edu

Aude Genevay

Massachusetts Institute of Technology
Cambridge, Massachusetts, USA
aude.genevay@gmail.com

Justin Solomon

Massachusetts Institute of Technology
Cambridge, Massachusetts, USA
jsolomon@mit.edu

Alexander Filippov

Huawei Noah's Ark Lab
Moscow, Russia
filippov.alexander@huawei.com

Evgeny Burnaev

Skolkovo Institute of Science and Technology
Moscow, Russia
e.burnaev@skoltech.ru

Abstract

Despite the recent popularity of neural network-based solvers for optimal transport (OT), there is no standard quantitative way to evaluate their performance. In this paper, we address this issue for quadratic-cost transport—specifically, computation of the Wasserstein-2 distance, a commonly-used formulation of optimal transport in machine learning. To overcome the challenge of computing ground truth transport maps between continuous measures needed to assess these solvers, we use input-convex neural networks (ICNN) to construct pairs of measures whose ground truth OT maps can be obtained analytically. This strategy yields pairs of continuous benchmark measures in high-dimensional spaces such as spaces of images. We thoroughly evaluate existing optimal transport solvers using these benchmark measures. Even though these solvers perform well in downstream tasks, many do not faithfully recover optimal transport maps. To investigate the cause of this discrepancy, we further test the solvers in a setting of image generation. Our study reveals crucial limitations of existing solvers and shows that increased OT accuracy does not necessarily correlate to better results downstream.

Solving optimal transport (OT) with continuous methods has become widespread in machine learning, including methods for large-scale OT [11, 36] and the popular Wasserstein Generative Adversarial Network (W-GAN) [3, 12]. Rather than discretizing the problem [31], continuous OT algorithms use neural networks or kernel expansions to estimate transport maps or dual solutions. This helps scale OT to large-scale and higher-dimensional problems not handled by discrete methods. Notable successes of continuous OT are in generative modeling [42, 20, 19, 7] and domain adaptation [43, 37, 25].

In these applications, OT is typically incorporated as part of the loss terms for a neural network model. For example, in W-GANs, the OT cost is used as a loss function for the generator; the model incorporates a neural network-based OT solver to estimate the loss. Although recent W-GANs provide state-of-the-art generative performance, however, it remains unclear to which extent this success is connected to OT. For example, [28, 32, 38] show that popular solvers for the Wasserstein-1 (\mathbb{W}_1) distance in GANs fail to estimate \mathbb{W}_1 accurately. While W-GANs were initially introduced

with \mathbb{W}_1 in [3], state-of-the art solvers now use both \mathbb{W}_1 and \mathbb{W}_2 (the *Wasserstein-2* distance, i.e., OT with the quadratic cost). While their experimental performance on GANs is similar, \mathbb{W}_2 solvers tend to converge faster (see [19, Table 4]) with better theoretical guarantees [19, 26, 16].

Contributions. In this paper, we develop a generic methodology for evaluating continuous quadratic-cost OT solvers (\mathbb{W}_2). Our main contributions are as follows:

- We use input-convex neural networks (ICNNs [2]) to construct pairs of continuous measures that we use as a benchmark with analytically-known solutions for quadratic-cost OT (§3, §4.1).
- We use these benchmark measures to evaluate popular quadratic-cost OT solvers in high-dimensional spaces (§4.3), including the image space of 64×64 CelebA faces (§4.4).
- We evaluate the performance of these OT solvers as a loss in generative modeling of images (§4.5).

Our experiments show that some OT solvers exhibit moderate error even in small dimensions (§4.3), performing similarly to trivial baselines (§4.2). The most successful solvers are those using parametrization via ICNNs. Surprisingly, however, solvers that faithfully recover \mathbb{W}_2 maps across dimensions struggle to achieve state-of-the-art performance in generative modeling.

Our benchmark measures can be used to evaluate future \mathbb{W}_2 solvers in high-dimensional spaces, a crucial step to improve the transparency and replicability of continuous OT research. Note the benchmark from [35] does not fulfill this purpose, since it is designed to test discrete OT methods and uses discrete low-dimensional measures with limited support.

Notation. We use $\mathcal{P}_2(\mathbb{R}^D)$ to denote the set of Borel probability measures on \mathbb{R}^D with finite second moment and $\mathcal{P}_{2,ac}(\mathbb{R}^D)$ to denote its subset of absolutely continuous probability measures. We denote by $\Pi(\mathbb{P}, \mathbb{Q})$ the set of the set of probability measures on $\mathbb{R}^D \times \mathbb{R}^D$ with marginals \mathbb{P} and \mathbb{Q} . For some measurable map $T : \mathbb{R}^D \rightarrow \mathbb{R}^D$, we denote by $T\#$ the associated push-forward operator. For $\phi : \mathbb{R}^D \rightarrow \mathbb{R}$, we denote by $\bar{\phi}$ its Legendre-Fenchel transform [10] defined by $\bar{\phi}(y) = \max_{x \in \mathbb{R}^D} [\langle x, y \rangle - \phi(x)]$. Recall that $\bar{\phi}$ is a convex function, even when ϕ is not.

1 Background on Optimal Transport

We start by stating the definition and some properties of optimal transport with quadratic cost. We refer the reader to [34, Chapter 1] for formal statements and proofs.

Primal formulation. For $\mathbb{P}, \mathbb{Q} \in \mathcal{P}_2(\mathbb{R}^D)$, Monge’s primal formulation of the squared *Wasserstein-2* distance, i.e., OT with quadratic cost, is given by

$$\mathbb{W}_2^2(\mathbb{P}, \mathbb{Q}) \stackrel{\text{def}}{=} \min_{T\#\mathbb{P}=\mathbb{Q}} \int_{\mathbb{R}^D} \frac{\|x - T(x)\|^2}{2} d\mathbb{P}(x), \quad (1)$$

where the minimum is taken over measurable functions (transport maps) $T : \mathbb{R}^D \rightarrow \mathbb{R}^D$ mapping \mathbb{P} to \mathbb{Q} . The optimal T^* is called the *optimal transport map* (OT map). Note that (1) is not symmetric, and this formulation does not allow for mass splitting, i.e., for some $\mathbb{P}, \mathbb{Q} \in \mathcal{P}_2(\mathbb{R}^D)$, there is no map T that satisfies $T\#\mathbb{P} = \mathbb{Q}$. Thus, Kantorovich proposed the following relaxation [14]:

$$\mathbb{W}_2^2(\mathbb{P}, \mathbb{Q}) \stackrel{\text{def}}{=} \min_{\pi \in \Pi(\mathbb{P}, \mathbb{Q})} \int_{\mathbb{R}^D \times \mathbb{R}^D} \frac{\|x - y\|^2}{2} d\pi(x, y), \quad (2)$$

where the minimum is taken over all transport plans π , i.e., measures on $\mathbb{R}^D \times \mathbb{R}^D$ whose marginals are \mathbb{P} and \mathbb{Q} . The optimal $\pi^* \in \Pi(\mathbb{P}, \mathbb{Q})$ is called the *optimal transport plan* (OT plan). If π^* is of the form $[\text{id}_{\mathbb{R}^D}, T^*]\#\mathbb{P} \in \Pi(\mathbb{P}, \mathbb{Q})$ for some T^* , then T^* is the minimizer of (1).

Dual formulation. For $\mathbb{P}, \mathbb{Q} \in \mathcal{P}_2(\mathbb{R}^D)$, the *dual formulation* of \mathbb{W}_2^2 is given by [40]:

$$\mathbb{W}_2^2(\mathbb{P}, \mathbb{Q}) = \max_{f \oplus g \leq \frac{1}{2}\|\cdot\|^2} \left[\int_{\mathbb{R}^D} f(x) d\mathbb{P}(x) + \int_{\mathbb{R}^D} g(y) d\mathbb{Q}(y) \right], \quad (3)$$

where the maximum is taken over all $f \in \mathcal{L}^1(\mathbb{P}, \mathbb{R}^D \rightarrow \mathbb{R})$ and $g \in \mathcal{L}^1(\mathbb{Q}, \mathbb{R}^D \rightarrow \mathbb{R})$ satisfying $f(x) + g(y) \leq \frac{1}{2}\|x - y\|^2$ for all $x, y \in \mathbb{R}^D$. From the optimal dual potential f^* , we can recover the optimal transport plan $T^*(x) = x - \nabla f^*(x)$ [34, Theorem 1.17].

The optimal f^*, g^* satisfy $(f^*)^c = g^*$ and $(g^*)^c = f^*$, where $u^c : \mathbb{R}^D \rightarrow \mathbb{R}$ is the c -transform of u defined by $u^c(y) = \min_{x \in \mathbb{R}^D} [1/2\|x - y\|^2 - u(x)]$. We can rewrite (3) as

$$\mathbb{W}_2^2(\mathbb{P}, \mathbb{Q}) = \max_f \left[\int_{\mathbb{R}^D} f(x) d\mathbb{P}(x) + \int_{\mathbb{R}^D} f^c(y) d\mathbb{Q}(y) \right], \quad (4)$$

where the maximum is taken over all $f \in \mathcal{L}^1(\mathbb{P}, \mathbb{R}^D \rightarrow \mathbb{R})$. Since f^* and g^* are each other's c -transforms, they are both c -concave [34, §1.6], which is equivalent to saying that functions $\psi^* : x \mapsto \frac{1}{2}\|x\|^2 - f^*(x)$ and $\phi^* : x \mapsto \frac{1}{2}\|x\|^2 - g^*(x)$ are convex [34, Proposition 1.21]. In particular, $\overline{\psi^*} = \phi^*$ and $\overline{\phi^*} = \psi^*$. Since

$$T^*(x) = x - \nabla f^*(x) = \nabla \left(\frac{\|x\|^2}{2} - f^*(x) \right) = \nabla \psi^*, \quad (5)$$

we see that the OT maps are gradients of convex functions, a fact known as Brenier's theorem [6].

“Solving” optimal transport problems. In applications, for given $\mathbb{P}, \mathbb{Q} \in \mathcal{P}_2(\mathbb{R}^D)$, the \mathbb{W}_2 optimal transport problem is typically considered in the following three similar but not equivalent tasks:

- **Evaluating $\mathbb{W}_2^2(\mathbb{P}, \mathbb{Q})$.** The Wasserstein-2 distance is a geometrically meaningful way to compare probability measures, providing a metric on $\mathcal{P}_2(\mathbb{R}^D)$.
- **Computing the optimal map T^* or plan π^* .** The map T^* provides an intuitive way to interpolate between measures. It is often used as a generative map between measures in problems like domain adaptation [36, 43] and image style transfer [16].
- **Using the gradient $\partial \mathbb{W}_2^2(\mathbb{P}_\alpha, \mathbb{Q}) / \partial \alpha$ to update generative models.** Derivatives of \mathbb{W}_2^2 are used implicitly in generative modeling that incorporates \mathbb{W}_2 loss [19, 33], in which case $\mathbb{P} = \mathbb{P}_\alpha$ is a parametric measure and \mathbb{Q} is the data measure. Typically, $\mathbb{P}_\alpha = G_\alpha \# \mathbb{S}$ is the measure generated from a fixed latent measure \mathbb{S} by a parameterized function G_α , e.g., a neural network. The goal is to find parameters α that minimize $\mathbb{W}_2^2(\mathbb{P}_\alpha, \mathbb{Q})$ via gradient descent.

In the generative model setting, by definition of the pushforward $\mathbb{P}_\alpha = G_\alpha \# \mathbb{S}$, we have

$$\mathbb{W}_2^2(\mathbb{P}_\alpha, \mathbb{Q}) = \int_z f^*(G_\alpha(z)) d\mathbb{S}(z) + \int_{\mathbb{R}^D} g^*(y) d\mathbb{Q}(y),$$

where f^* and g^* are the optimal dual potentials. At each generator training step, f^* and g^* are fixed so that when we take the gradient with respect to α , by applying the chain rule we have:

$$\frac{\partial \mathbb{W}_2^2(\mathbb{P}_\alpha, \mathbb{Q})}{\partial \alpha} = \int_z \mathbf{J}_\alpha G_\alpha(z)^T \nabla f^*(G_\alpha(z)) d\mathbb{S}(z), \quad (6)$$

where $\mathbf{J}_\alpha G_\alpha(z)^T$ is the transpose of the Jacobian matrix of $G_\alpha(z)$ w.r.t. parameters α . This result still holds without assuming the potentials are fixed by the envelope theorem [29]. To capture the gradient, we need a good estimate of $\nabla f^* = \text{id}_{\mathbb{R}^D} - T^*$ by (5). This task is somewhat different from computing the OT map T^* : since the estimate of ∇f^* is only involved in the gradient update for the generator, it is allowed to differ while still resulting in a good generative model.

We will use the generic phrase *OT solver* to refer to a method for solving any of the tasks above.

Quantitative evaluation of OT solvers. For discrete OT methods, a benchmark dataset [35] exists but the mechanism for producing the dataset does not extend to continuous OT. Existing continuous solvers are typically evaluated on a set of self-generated examples or tested in generative models without evaluating its actual OT performance. Two kinds of metrics are often used:

Direct metrics compare the computed transport map \hat{T} with the true one T^* , e.g., by using \mathcal{L}^2 Unexplained Variance Percentage (\mathcal{L}^2 -UVP) metric [16, §5.1], [17, §5]. There are relatively few direct metrics available, since the number of examples of \mathbb{P}, \mathbb{Q} with known ground truth T^* is small: it is known that T^* can be analytically derived or explicitly computed in the discrete case [31, §3], 1-dimensional case [31, §2.6], and Gaussian/location-scatter cases [1].

Indirect metrics use an OT solver as a component in a larger pipeline, using end-to-end performance as a proxy for solver quality. For example, in generative modeling where OT is used as the generator loss [19, 27], the quality of the generator can be assessed through metrics for GANs, such as the Fréchet Inception distance (FID) [13]. Indirect metrics do not provide clear understanding about the quality of the solver itself, since they depend on components of the model that are not related to OT.

2 Continuous Dual Solvers for Quadratic Cost Transport

While our benchmark might be used to test any continuous solver which computes map T^* or gradient ∇f^* , in this paper, we perform evaluation only on *dual-form* continuous solvers based on (3) or (4). Such solvers have straightforward optimization procedures and can be adapted to various datasets without extensive hyperparameter search. In contrast, *primal-form* solvers based on (1), e.g., [18, 43, 21, 23], typically parameterize T^* using complicated generative modeling techniques that depend on careful hyperparameter search and complex optimization procedures [24].

We summarize existing continuous dual form solvers in Table 1. These fit a parametric function f_θ (or ψ_θ) to approximate f^* (or $\psi^* = \text{id}_{\mathbb{R}^D} - f^*$). The resulting f_θ produces an approximate OT map $\text{id}_{\mathbb{R}^D} - \nabla f_\theta = \nabla \psi_\theta \approx T^*$ and derivative $\nabla f_\theta = \text{id}_{\mathbb{R}^D} - \nabla \psi_\theta$ needed to update generative models (6).

| Solver | Related works | Parameterization of potentials or maps | Quantitatively tested as OT | Tested in GANs |
|-----------------------------|---------------|---|-----------------------------|----------------------------|
| Regularized [LS] | [11, 36, 33] | $f_\theta, g_\omega : \mathbb{R}^D \rightarrow \mathbb{R}$ - NNs | Gaussian case [16] | Ent.-regularized WGAN [33] |
| Maximin [MM] | [30] | $f_\theta : \mathbb{R}^D \rightarrow \mathbb{R}$ - NN $H_\omega : \mathbb{R}^D \rightarrow \mathbb{R}^D$ - NN | ✗ | Three-player WGAN [30] |
| Maximin (Batch-wise) [MM-B] | [27, 8] | $f_\theta : \mathbb{R}^D \rightarrow \mathbb{R}$ - NN | ✗ | (q,p)-WGAN [27] |
| Quadratic Cost [QC] | [19] | $f_\theta : \mathbb{R}^D \rightarrow \mathbb{R}$ - NN | ✗ | WGAN-QC [19] |
| Maximin + ICNN [MMv1] | [39] | $\psi_\theta : \mathbb{R}^D \rightarrow \mathbb{R}$ - ICNN | Gaussian case [16] | ✗ |
| Maximin + 2 ICNNs [MMv2] | [26, 9] | $\psi_\theta : \mathbb{R}^D \rightarrow \mathbb{R}$ - ICNN $H_\omega : \mathbb{R}^D \rightarrow \mathbb{R}^D - \nabla \text{ICNN}$ | Gaussian case [16] | ✗ |
| Non-Maximin [W2] | [16, 17] | $\psi_\theta : \mathbb{R}^D \rightarrow \mathbb{R}$ - ICNN $H_\omega : \mathbb{R}^D \rightarrow \mathbb{R}^D - \nabla \text{ICNN}$ | Gaussian case [16] | ✗ |

Table 1: Comprehensive table of existing continuous dual solvers for OT with the quadratic cost.

To our knowledge, none of these solvers has been quantitatively evaluated in a non-Gaussian setting. For [MM], [MM-B], and [QC], the quality of the recovered derivatives ∇f^* for $\partial \mathbb{W}_2^2(\mathbb{P}_\alpha, \mathbb{Q}) / \partial \alpha$ has only been evaluated implicitly through GAN metrics. Moreover, these three solvers have not been quantitatively evaluated on solving OT tasks. We now overview each solver from Table 1.

[LS] optimizes an unconstrained regularized dual form of (3) [36]:

$$\max_{f, g} \left[\int_{\mathbb{R}^D} f(x) d\mathbb{P}(x) + \int_{\mathbb{R}^D} g(y) d\mathbb{Q}(y) \right] - \mathcal{R}(f, g). \quad (7)$$

The *entropic* or *quadratic* regularizer \mathcal{R} penalizes potentials f, g for violating the constraint $f \oplus g \leq \frac{1}{2} \|\cdot\|^2$ [36, §3]. In practice, $f = f_\theta$ and $g = g_\omega$ are linear combinations of kernel functions [11] or neural networks [36]. The parameters θ, ω are obtained by applying stochastic gradient ascent (SGA) over random mini-batches sampled from \mathbb{P}, \mathbb{Q} .

Most other solvers are based on an expansion of (4):

$$\mathbb{W}_2^2(\mathbb{P}, \mathbb{Q}) = \max_f \int_{\mathbb{R}^D} f(x) d\mathbb{P}(x) + \int_{\mathbb{R}^D} \overbrace{\min_{x \in \mathbb{R}^D} \left[\frac{1}{2} \|x - y\|^2 - f(x) \right]}^{=f^c(y)} d\mathbb{Q}(y). \quad (8)$$

The challenge of (8) is the inner minimization over $x \in \mathbb{R}^D$, i.e., evaluating $f^c(y)$. The main difference between existing solvers is the procedure used to solve this inner problem.

[MM-B] uses a neural network f_θ as the potential trained using mini-batch SGA [27]. To solve the inner problem, the authors restrict the minimization of x to the current mini-batch from \mathbb{P} instead of \mathbb{R}^D . The strategy is fast but leads to *overestimation* of the inner problem’s solution since the minimum is taken over a restricted subset.

[MM-v1] exploits the property that $f^* = \frac{1}{2} \|\cdot\|^2 - \psi^*$, where ψ^* is convex [39]. The authors parametrize $f_\theta = \frac{1}{2} \|\cdot\|^2 - \psi_\theta$, where ψ_θ is an input convex neural network (ICNN) [2]. Hence, for every $y \in \mathbb{R}^D$, the inner problem of (8) becomes convex in x . This problem can be solved using SGA to high precision, but doing so is computationally costly [16, §C.4].

[MM] uses a formulation equivalent to (8) [30]:

$$\mathbb{W}_2^2(\mathbb{P}, \mathbb{Q}) = \max_f \int_{\mathbb{R}^D} f(x) d\mathbb{P}(x) + \int_{\mathbb{R}^D} \min_H \left[\frac{1}{2} \|H(y) - y\|^2 - f(H(y)) \right] d\mathbb{Q}(y), \quad (9)$$

where the minimization is performed over functions $H : \mathbb{R}^D \rightarrow \mathbb{R}^D$. The authors use neural networks f_θ and H_ω to parametrize the potential and the minimizer of the inner problem. To train θ, ω , the authors apply stochastic gradient ascent/descent (SGAD) over mini-batches from \mathbb{P}, \mathbb{Q} . [MM] is generic and can be modified to compute arbitrary transport costs and derivatives, not just \mathbb{W}_2^2 , although the authors have tested only on the Wasserstein-1 (\mathbb{W}_1) distance.

Similarly to [MMv1], [MMv2] parametrizes $f_\theta = \frac{1}{2} \|\cdot\|^2 - \psi_\theta$, where ψ_θ is an ICNN [26]. For a fixed f_θ , the optimal solution H is given by $H = (\nabla \psi_\theta)^{-1}$ which is an inverse gradient of a convex function, so it is also a gradient of a convex function. Hence, the authors parametrize $H_\omega = \nabla \phi_\omega$, where ϕ_ω is an ICNN, and use [MM] to fit θ, ω .

[W2] uses the same ICNN parametrization as [26] but introduces *cycle-consistency* regularization to avoid solving a maximin problem [16, §4].

Finally, we highlight the solver [QC] [19]. Similarly to [MM-B], a neural network f_θ is used as the potential. When each pair of mini-batches $\{x_n\}, \{y_n\}$ from \mathbb{P}, \mathbb{Q} is sampled, the authors solve a *discrete* OT problem to obtain dual variables $\{f_n^*\}, \{g_n^*\}$, which are used to regress $f_\theta(x_n)$ onto f_n^* .

Gradient deviation. The solvers above optimize for potentials like f_θ (or ψ_θ), but it is the gradient of f_θ (or ψ_θ) that is used to recover the OT map via $T = x - \nabla f_\theta$. Even if $\|f - f^*\|_{\mathcal{L}^2(\mathbb{P})}^2$ is small, the difference $\|\nabla f_\theta - \nabla f^*\|_{\mathcal{L}^2(\mathbb{P})}^2$ may be arbitrarily large since ∇f_θ is not directly involved in optimization process. We call this issue *gradient deviation*. This issue is only addressed formally for ICNN-based solvers [MMv1], [MMv2], [W2] [16, Theorem 4.1], [26, Theorem 3.6].

Reversed solvers. [MM], [MMv2], [W2] recover not only the forward OT map $\nabla \psi_\theta \approx \nabla \psi^* = T^*$, but also the inverse, given by $H_\omega \approx (T^*)^{-1} = (\nabla \psi^*)^{-1} = \nabla \psi^*$, see [26, §3] or [16, §4.1]. These solvers are asymmetric in \mathbb{P}, \mathbb{Q} and an alternative is to swap \mathbb{P} and \mathbb{Q} during training. We denote such *reversed* solvers by [MM:R], [MMv2:R], [W2:R]. In §4 we show that surprisingly [MM:R] works better in generative modeling than [MM].

3 Benchmarking OT Solvers

In this section, we develop a generic method to produce *benchmark pairs*, i.e., measures (\mathbb{P}, \mathbb{Q}) such that $\mathbb{Q} = T\#\mathbb{P}$ with sample access and an analytically known OT solution T^* between them.

Key idea. Our method is based on the fact that for a differentiable convex function $\psi : \mathbb{R}^D \rightarrow \mathbb{R}$, its gradient $\nabla \psi$ is an *optimal* transport map between any $\mathbb{P} \in \mathcal{P}_{2,ac}(\mathbb{R}^D)$ and its pushforward $\nabla \psi\#\mathbb{P}$ by $\nabla \psi : \mathbb{R}^D \rightarrow \mathbb{R}^D$. This follows from Brenier’s theorem [6], [41, Theorem 2.12]. Thus, for a continuous measure \mathbb{P} with sample access and a *known* convex ψ , $(\mathbb{P}, \nabla \psi\#\mathbb{P})$ can be used as a benchmark pair. We sample from $\nabla \psi\#\mathbb{P}$ by drawing samples from \mathbb{P} and pushing forward by $\nabla \psi$.

Arbitrary pairs (\mathbb{P}, \mathbb{Q}) . It is difficult to compute the exact continuous OT solution for an arbitrary pair (\mathbb{P}, \mathbb{Q}) . As a compromise, we compute an *approximate* transport map as the gradient of an ICNN using [W2]. That is, we find ψ_θ parameterized as an ICNN such that $\nabla \psi_\theta\#\mathbb{P} \approx \mathbb{Q}$. Then, the modified pair $(\mathbb{P}, \nabla \psi_\theta\#\mathbb{P})$ can be used to benchmark OT solvers. We choose [W2] because it exhibits good performance in higher dimensions, but other solvers can also be used so long as ψ_θ is convex. Because of the choice of [W2], subsequent evaluation might slightly favor ICNN-based methods.

Extensions. Convex functions can be modified to produce more benchmark pairs. If ψ_1, \dots, ψ_N are convex, then $\sigma(\psi_1, \dots, \psi_N)$ is convex when $\sigma : \mathbb{R}^N \rightarrow \mathbb{R}$ is convex and monotone. For example, $c \cdot \psi_1$ ($c \geq 0$), $\sum_n \psi_n$, $\max_n \psi_n$ are convex, and their gradients produce new benchmark pairs.

Inversion. If $\nabla \psi_\theta$ is bijective, then the inverse transport map for $(\mathbb{P}, \nabla \psi_\theta\#\mathbb{P})$ exists and is given by $(\nabla \psi_\theta)^{-1}$. For each $y \in \mathbb{R}^D$, the value $(\nabla \psi_\theta)^{-1}(y)$ can be obtained by solving a *convex* problem [39, §6], [16, §3]. All ICNNs ψ_θ we use have bijective gradients $\nabla \psi_\theta$, as detailed in Appendix B.1.

4 Benchmark Details and Results

We implement our benchmark in PyTorch and will release pre-trained transport maps for all benchmark pairs. The experiments are conducted on 4 GTX 1080ti GPUs and require about 100 hours of computation (per GPU). We provide implementation details in Appendix B.

4.1 Datasets

High-dimensional measures. We develop benchmark pairs to test whether the OT solvers can redistribute mass among modes of measures. For this purpose, we use Gaussian mixtures in dimensions $D = 2^1, 2^2, \dots, 2^8$. In each dimension D , we consider a random mixture \mathbb{P} of 3 Gaussians and two random mixtures $\mathbb{Q}_1, \mathbb{Q}_2$ of 10 Gaussians. We train approximate transport maps $\nabla\psi_i \# \mathbb{P} \approx \mathbb{Q}_i$ ($i = 1, 2$) using the [W2] solver. Each potential is an ICNN with DenseICNN architecture [16, §B.2]. We create a benchmark pair via the half-sum of computed potentials ($\mathbb{P}, \frac{1}{2}(\nabla\psi_1 + \nabla\psi_2) \# \mathbb{P}$). The first measure \mathbb{P} is a mixture of 3 Gaussians and the second is obtained by averaging potentials, which transforms it to approximate mixtures of 10 Gaussians. See Appendix A.1 and Figure 4 for details.

Images. We use the aligned images of CelebA64 faces dataset¹ [22] to produce additional benchmark pairs. First, we fit 3 generative models (WGAN-QC [19]) on the dataset and pick intermediate training checkpoints to produce continuous measures $\mathbb{Q}_{\text{Early}}^k, \mathbb{Q}_{\text{Mid}}^k, \mathbb{Q}_{\text{Late}}^k$ for the first 2 models ($k = 1, 2$) and the final checkpoint of the third model ($k = 3$) to produce measure $\mathbb{P}_{\text{Final}}^3$. To make measures absolutely continuous, we add small Gaussian noise to the generator’s output. Each checkpoint (Early, Mid, Late, Final) represents images of faces of a particular quality. Next, for $k \in \{1, 2\}$ and $\text{Cpkt} \in \{\text{Early}, \text{Mid}, \text{Late}\}$, we use [W2] solver to fit an approximate transport map $\nabla\psi_{\text{Cpkt}}^k$ for the pair $(\mathbb{P}_{\text{Final}}^3, \mathbb{Q}_{\text{Cpkt}}^k)$, i.e., $\nabla\psi_{\text{Cpkt}}^k \# \mathbb{P}_{\text{Final}}^3 \approx \mathbb{Q}_{\text{Cpkt}}^k$. The potential ψ_{Cpkt}^k is a convolutional ICNN with ConvICNN64 architecture (§B.1). For each Cpkt, we define a benchmark pair $(\mathbb{P}_{\text{CelebA}}, \mathbb{Q}_{\text{Cpkt}}) \stackrel{\text{def}}{=} (\mathbb{P}_{\text{Final}}^3, [(\nabla\psi_{\text{Cpkt}}^1 + \nabla\psi_{\text{Cpkt}}^2)/2] \# \mathbb{P}_{\text{Final}}^3)$. See Appendix A.2 and Figure 6 for details.

4.2 Metrics and Baselines

Baselines. We propose three baseline methods: identity [ID], constant [C] and linear [L]. The *identity* solver outputs $T^{\text{id}} = \text{id}_{\mathbb{R}^D}$ as the transport map. The *constant* solver outputs the mean value of \mathbb{Q} , i.e., $T^0 \equiv \mathbb{E}_{\mathbb{Q}}[y] \equiv \mu_{\mathbb{Q}}$. The *linear* solver outputs $T^1(x) = \Sigma_{\mathbb{P}}^{-\frac{1}{2}} (\Sigma_{\mathbb{P}}^{\frac{1}{2}} \Sigma_{\mathbb{Q}} \Sigma_{\mathbb{P}}^{\frac{1}{2}})^{\frac{1}{2}} \Sigma_{\mathbb{P}}^{-\frac{1}{2}} (x - \mu_{\mathbb{P}}) + \mu_{\mathbb{Q}}$, i.e., the OT map between measures coarsened to Gaussians [1, Theorem 2.3].

Metrics. To assess the quality of the recovered transport map $\hat{T} : \mathbb{R}^D \rightarrow \mathbb{R}^D$ from \mathbb{P} to \mathbb{Q} , we use *unexplained variance percentage* (UVP) [16]: $\mathcal{L}^2\text{-UVP}(\hat{T}) \stackrel{\text{def}}{=} 100 \cdot \|\hat{T} - T^*\|_{\mathcal{L}^2(\mathbb{P})}^2 / \text{Var}(\mathbb{Q})\%$. Here T^* is the OT map. For values $\approx 0\%$, \hat{T} approximates T^* well. For values $\geq 100\%$, map \hat{T} is far from optimal. The constant baseline provides $\mathcal{L}^2\text{-UVP}(T^0) = 100\%$.

To measure the quality of approximation of the derivative of the potential $[\text{id}_{\mathbb{R}^D} - \hat{T}] \approx \nabla f^*$ that is used to update generative models (6), we use *cosine similarity* (cos):

$$\cos(\text{id} - \hat{T}, \text{id} - T^*) \stackrel{\text{def}}{=} \frac{\langle \hat{T} - \text{id}, \nabla\psi^* - \text{id} \rangle_{\mathcal{L}^2(\mathbb{P})}}{\|T^* - \text{id}\|_{\mathcal{L}^2(\mathbb{P})} \cdot \|\hat{T} - \text{id}\|_{\mathcal{L}^2(\mathbb{P})}} \in [-1, 1].$$

To estimate $\mathcal{L}^2\text{-UVP}$ and cos metrics, we use 2^{14} random samples from \mathbb{P} .

4.3 Evaluation of Solvers on High-dimensional Benchmark Pairs

We evaluate the solvers on the benchmark and report the computed metric values for the fitted transport map. For fair comparison, in each method the potential f and the map H (where applicable) are parametrized as $f_{\theta} = \frac{1}{2} \|\cdot\|^2 - \psi_{\theta}$ and $H_{\omega} = \nabla\phi_{\omega}$ respectively, where $\psi_{\theta}, \phi_{\omega}$ use DenseICNN architectures [16, §B.2]. In solvers [QC], [LS], [MM-B], [MM] we do not impose any restrictions on the weights θ, ω , i.e. $\psi_{\theta}, \phi_{\omega}$ are usual fully connected nets with additional skip connections. We provide the computed metric values in Table 2 and visualize fitted maps (for $D = 64$) in Figure 1.

All the solvers perform well ($\mathcal{L}^2\text{-UVP} \approx 0$, $\cos \approx 1$) in dimension $D = 2$. In higher dimensions, only [MMv1], [MM], [MMv2], [W2] and their reversed versions produce reasonable results. However, [MMv1] solver is slow since each optimization step solves a hard subproblem for computing f^c . Maximin solvers [MM], [MMv2], [MM:R] are also hard to optimize: they either diverge from the start (\rightarrow) or diverge after converging to nearly-optimal saddle point (\rightarrow). This behavior is typical for maximin optimization and possibly can be avoided by a more careful choice of hyperparameters.

For [QC], [LS], [MM-B], as the dimension increases, the $\mathcal{L}^2\text{-UVP}$ drastically grows. Only [MM-B] notably outperforms the trivial [L] baseline. The error of [MM-B] is explained by the overestimation

¹<http://mmlab.ie.cuhk.edu.hk/projects/CelebA.html>

of the inner problem in (8), yielding biased optimal potentials. The error of [LS] comes from bias introduced by regularization [36]. In [QC], error arises because a discrete OT problem solved on sampled mini-batches, which is typically biased [5, Theorem 1], is used to update f_θ . Interestingly, although [QC], [LS] are imprecise in terms of \mathcal{L}^2 -UVP, they provide a high cos metric.

Due to optimization issues and performance differences, wall-clock times for convergence are not representative. All solvers except [MMv1] converged in several hours. Among solvers that substantially outperform the linear baseline, i.e. [MM], [MMv1], [MMv2], [W2], [MM-B], the fastest converging one is [MM-B], but it is biased. [MM], [MMv2], [W2] require more time.

| Dim | 2 | 4 | 8 | 16 | 32 | 64 | 128 | 256 |
|----------|------|------|------|------|------|--------|-------|-------|
| [MMv1] | 0.2 | 1.0 | 1.8 | 1.4 | 6.9 | 8.1 | 2.2 | 2.6 |
| [MM] | 0.1 | 0.3 | 0.9 | 2.2 | 4.2 | 3.2 | 3.1q→ | 4.1q→ |
| [MM:R] | 0.1 | 0.3 | 0.7 | 1.9 | 2.8 | 4.5 | →→ | →→ |
| [MMv2] | 0.1 | 0.68 | 2.2 | 3.1 | 5.3 | 10.1q→ | 3.2q→ | 2.7q→ |
| [MMv2:R] | 0.1 | 0.7 | 4.4 | 7.7 | 5.8 | 6.8 | 2.1 | 2.8 |
| [W2] | 0.1 | 0.7 | 2.6 | 3.3 | 6.0 | 7.2 | 2.0 | 2.7 |
| [W2:R] | 0.2 | 0.9 | 4.0 | 5.3 | 5.2 | 7.0 | 2.0 | 2.7 |
| [MM-B] | 0.1 | 0.7 | 3.1 | 6.4 | 12.0 | 13.9 | 19.0 | 22.5 |
| [LS] | 5.0 | 11.6 | 21.5 | 31.7 | 42.1 | 40.1 | 46.8 | 54.7 |
| [L] | 14.1 | 14.9 | 27.3 | 41.6 | 55.3 | 63.9 | 63.6 | 67.4 |
| [QC] | 1.5 | 14.5 | 28.6 | 47.2 | 64.0 | 75.2 | 80.5 | 88.2 |
| [C] | 100 | 100 | 100 | 100 | 100 | 100 | 100 | 100 |
| [ID] | 32.7 | 42.0 | 58.6 | 87 | 121 | 137 | 145 | 153 |

| Dim | 2 | 4 | 8 | 16 | 32 | 64 | 128 | 256 |
|----------|------|------|------|------|------|--------|--------|--------|
| [MMv1] | 0.99 | 0.99 | 0.99 | 0.99 | 0.98 | 0.97 | 0.99 | 0.99 |
| [MM] | 0.99 | 0.99 | 0.99 | 0.99 | 0.99 | 0.99 | 0.99q→ | 0.99q→ |
| [MM:R] | 0.99 | 1.00 | 1.00 | 0.99 | 1.00 | 0.98 | →→ | →→ |
| [MMv2] | 0.99 | 0.99 | 0.99 | 0.99 | 0.99 | 0.96q→ | 0.99q→ | 0.99q→ |
| [MMv2:R] | 0.99 | 1.00 | 0.97 | 0.96 | 0.99 | 0.97 | 0.99 | 1.00 |
| [W2] | 0.99 | 0.99 | 0.99 | 0.99 | 0.99 | 0.97 | 1.00 | 1.00 |
| [W2:R] | 0.99 | 1.00 | 0.98 | 0.98 | 0.99 | 0.97 | 1.00 | 1.00 |
| [MM-B] | 0.99 | 1.00 | 0.98 | 0.96 | 0.96 | 0.94 | 0.93 | 0.93 |
| [LS] | 0.94 | 0.86 | 0.80 | 0.80 | 0.81 | 0.83 | 0.82 | 0.81 |
| [L] | 0.75 | 0.80 | 0.73 | 0.73 | 0.76 | 0.75 | 0.77 | 0.77 |
| [QC] | 0.99 | 0.84 | 0.78 | 0.70 | 0.70 | 0.70 | 0.69 | 0.66 |
| [C] | 0.29 | 0.32 | 0.38 | 0.46 | 0.55 | 0.58 | 0.60 | 0.62 |
| [ID] | 0.00 | 0.00 | 0.00 | 0.00 | 0.00 | 0.00 | 0.00 | 0.00 |

Table 2: \mathcal{L}^2 -UVP (% , on the left) and $\cos \in [-1, 1]$ (on the right) metric values for transport maps fitted by OT solvers on the high-dimensional benchmark in dimensions $D = 2, 2^2, \dots, 2^8$. **Orange** highlights \mathcal{L}^2 -UVP $> 10\%$ and $\cos < 0.95$. **Red** indicates performance worse than [L] baseline.

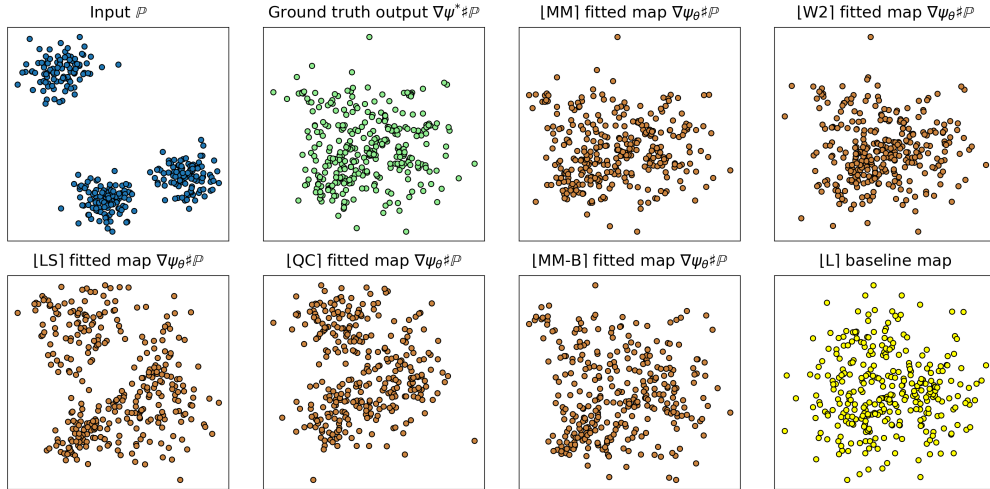


Figure 1: Visualization of a 64-dimensional benchmark pair and OT maps fitted by the solvers. Scatter plots contain 512 random samples projected onto 2 principal components of measure $\nabla\psi^*\#\mathbb{P}$.

4.4 Evaluation of Solvers in CelebA 64×64 Images Benchmark Pairs

For evaluation on the CelebA benchmark, we excluded [LS] and [MMv1]: the first is unstable in high dimensions [33], and the second takes too long to converge. ICNN-based solvers [MMv2], [W2] and their reversed versions perform roughly the same in this experiment. For simplicity, we treat them as one solver [W2].

In [W2], we parametrize $f_\theta = \frac{1}{2}\|\cdot\|^2 - \psi_\theta$ and $H_\omega = \nabla\phi_\omega$, where ψ_θ, ϕ_ω are input-convex neural nets with ConvexICNN64 architecture (§B.1). All the other solvers are designed in the generative modeling setting to work with convolutional architectures for images. Thus, in [MM], [QC], [MM-B] we parametrize networks f_θ as ResNet and H_ω as U-Net (in [MM]). In turn, in [MM:R] we parametrize T_θ by UNet and g_ω by ResNet.

We compute the transport map $\mathbb{Q}_{\text{Cpkt}} \rightarrow \mathbb{P}_{\text{CelebA}}$ for each solver on three image benchmarks. The results are in Figure 2 and Table 3 and echo patterns observed on high-dimensional problems (§4.3). [QC], [MM-B] suffer from extreme bias thanks to the high dimension of images, and the derivative of \mathbb{W}_2^2 computed by these solvers is almost orthogonal to the true derivative ($\cos \approx 0$). This means

that *these solvers do not extract* \mathbb{W}_2^2 . [MM], [MM:R], [W2] recover the transport maps well. [MM]’s map is slightly noisier than the one by [MM:R], a minor example of gradient deviation.

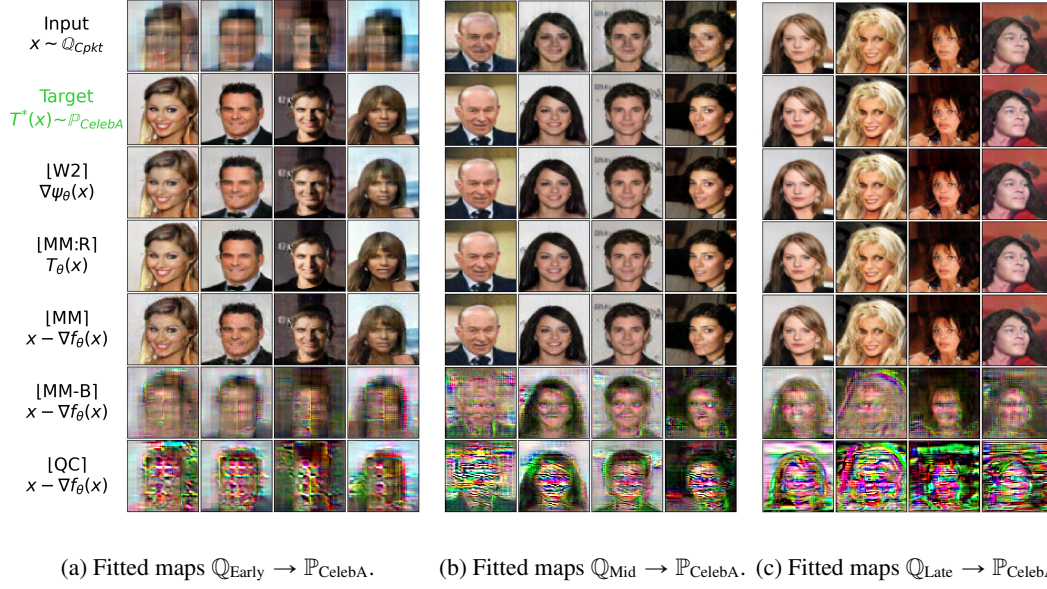


Figure 2: OT maps fitted by solvers on benchmarks ($\mathbb{Q}_{\text{Cpkt}}, \mathbb{P}_{\text{CelebA}}$). 1st line contains random $x \sim \mathbb{Q}_{\text{Cpkt}}$. 2nd line contains samples from $\mathbb{P}_{\text{CelebA}}$ obtained by pushing x forward by OT map $T^* = \nabla \psi^*$. Subsequent lines show x transported by maps fitted by OT solvers.

| Cpkt | Early | Mid | Late |
|--------|-------------|----------------|----------------|
| [W2] | 1.7 | 0.5 | 0.25 |
| [MM] | 2.2 | 0.9 | 0.53 |
| [MM:R] | 1.4 | 0.4 | 0.22 |
| [ID] | 31.2 | 4.26 | 2.06 |
| [MM-B] | 45.9 | 46.1 | 47.74 |
| [C] | 100 | 100 | 100 |
| [QC] | 94.7 | >100 | >100 |

| Cpkt | Early | Mid | Late |
|--------|-------------|--------------|--------------|
| [W2] | 0.99 | 0.95 | 0.93 |
| [MM] | 0.98 | 0.90 | 0.87 |
| [MM:R] | 0.99 | 0.96 | 0.94 |
| [ID] | 0.00 | 0.00 | 0.00 |
| [MM-B] | 0.28 | -0.08 | -0.14 |
| [C] | 0.03 | -0.14 | -0.20 |
| [QC] | 0.17 | -0.01 | 0.05 |

Table 3: \mathcal{L}^2 -UVP (% , on the left) and $\cos \in [-1, 1]$ (on the right) metric values for transport maps $\mathbb{Q}_{\text{Cpkt}} \rightarrow \mathbb{P}_{\text{CelebA}}$ fitted by OT solvers on 3 developed CelebA64 \mathbb{W}_2 benchmarks.

4.5 Evaluation of Solvers in Generative Modeling of CelebA 64×64 Faces

Based on our previous evaluation, many existing neural OT solvers are notably imprecise. This leads us to ask: *To what extent does solver quality matter in real-world applications?*

To address this question, we evaluate the most promising solvers in the task of generative modeling for CelebA 64×64 images of faces. For comparison, we add [QC], which has good generative performance [19]. For each solver, we train a generative network G_α with ResNet architecture from [19] to map a 128-dimensional normal distribution \mathbb{S} to the data distribution \mathbb{Q} . As the loss function for generator, we use $\mathbb{W}_2^2(\mathbb{P}_\alpha, \mathbb{Q}) = \mathbb{W}_2^2(G_\alpha \# \mathbb{S}, \mathbb{Q})$ estimated by each solver. We perform GAN-style training, where gradient updates of the generator alternate with gradient steps of OT solver (discriminator) (§B.2.3). We show sample generated images in the top row of each subplot of Figure 3 and report FID [13]. On the bottom row, we show the pushforward of the OT map from $\mathbb{P}_\alpha = G_\alpha \# \mathbb{S}$ to \mathbb{Q} extracted from the OT solver. Since the model converged ($\mathbb{P}_\alpha \approx \mathbb{Q}$), the map should be nearly equal to the identity.

[W2] provides the least quality (Figure 3a). This can be explained by the use of ConvICNN: the other solvers use convolutional architectures and work better. In general, the applicability of ICNNs to image-based tasks is questionable [16, §5.3] which might be a serious practical limitation.

[QC] has strong generative performance (Figure 3b). However, as in §4.3-4.4, the recovered map is far from the identity. We suspect this solver has decent generative performance because it approximates some non- \mathbb{W}_2^2 dissimilarity measure in practice.

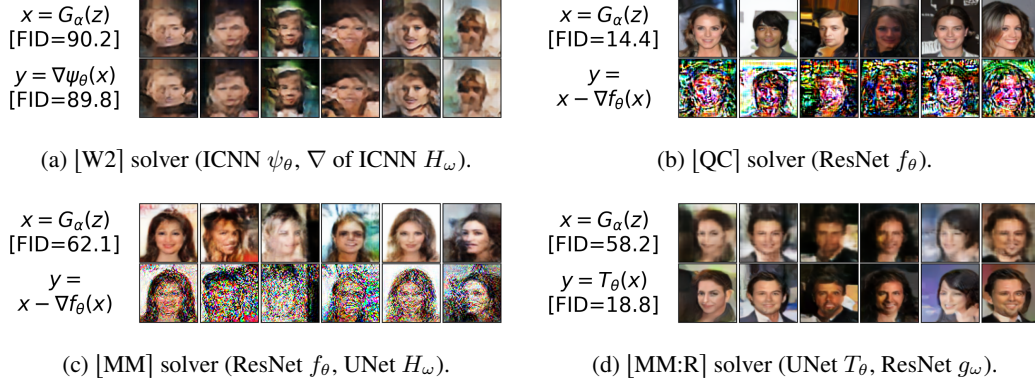


Figure 3: Random images produced by trained generative models with OT solvers. The 1st line shows random generated images $x = G_\alpha(z) \sim \mathbb{P}_\alpha$, $z \sim \mathbb{S}$. The 2nd line shows computed transport map from the generated $x = G_\alpha(z) \sim \mathbb{P}_\alpha$ to the data distribution \mathbb{Q} .

[MM] results in a generative model that produces blurry images (Figure 3c). The computed transport map $\text{id}_{\mathbb{R}^D} - \nabla f_\theta$ is too far from the identity due to the gradient deviation. This leads to inaccurate gradient computation used to update the generator and explains why the generator struggles to improve. We emphasize that in §4.4 [MM] does not notably suffer from the gradient deviation. Probably, this is due to measures being absolutely continuous and supported on the entire \mathbb{R}^D . This is not the case in our generative modeling setup, where generated and data measures are supported on low-dimensional manifolds in \mathbb{R}^D .

Reversed [MM:R] overcomes the problem of [MM] with the gradient deviation but still leads to blurry images (Figure 3d). Interestingly, the fitted transport map T_θ significantly improves the quality and images $T_\theta \circ G_\alpha(z)$ are comparable to the ones with [QC] solver (Figure 3b).

We emphasize that formulations from [MM], [MM:R] solvers are maximin: using them in GANs requires solving a challenging *min-max-min* optimization problem. To handle this, we use three nested loops and stochastic gradient descent-ascent-descent. In our experiments, the training was not stable and often diverged: the reported results use the best hyperparameters we found, although there may exist better ones. The difficulty in selecting hyperparameters and the unstable training process are limitations of these solvers that need to be addressed before using in practice.

5 Conclusion

Our methodology creates pairs of continuous measures with ground truth quadratic-cost optimal transport maps, filling the missing gap of benchmarking continuous OT solvers. This development allows us to evaluate the performance of quadratic-cost OT solvers in OT-related tasks. Beyond benchmarking the basic transport problem, our study of generative modeling reveals surprising patterns: bad OT solvers can yield good generative performance, and simply reversing asymmetric solvers can affect performance dramatically.

Limitations. We rely on ICNN gradients as \mathbb{W}_2 optimal transport maps to generate pairs of benchmark measures. It is unclear whether analogous constructions can be used for other costs such as \mathbb{W}_1 . We also limit our benchmark pairs to be absolutely continuous measures while limiting the ground truth transport maps to be gradients of ICNNs, which may not have enough representational power. While we reveal a discrepancy between performance in OT-related tasks and performance in generative modeling, in-depth study is needed to answer questions such as what exact dissimilarity metric [QC] implies that explains its generative performance while poorly approximating \mathbb{W}_2 .

Potential impact. We expect our benchmark to become a standard benchmark for continuous optimal transport as part of the ongoing effort of advancing computational OT, in particular, in its application to generative modeling. As a result, we hope our work can improve the quality and reusability of OT-related research. One potential negative is that our benchmark might narrow the evaluation of future OT solvers to the datasets of our benchmark. To avoid this, besides particular benchmark datasets, in §3 we describe a generic method to produce new benchmark pairs.

References

- [1] Pedro C Álvarez-Esteban, E Del Barrio, JA Cuesta-Albertos, and C Matrán. A fixed-point approach to barycenters in Wasserstein space. *Journal of Mathematical Analysis and Applications*, 441(2):744–762, 2016.
- [2] Brandon Amos, Lei Xu, and J Zico Kolter. Input convex neural networks. In *Proceedings of the 34th International Conference on Machine Learning-Volume 70*, pages 146–155. JMLR. org, 2017.
- [3] Martin Arjovsky, Soumith Chintala, and Léon Bottou. Wasserstein GAN. *arXiv preprint arXiv:1701.07875*, 2017.
- [4] Jonathan T Barron. Continuously differentiable exponential linear units. *arXiv preprint arXiv:1704.07483*, 2017.
- [5] Marc G Bellemare, Ivo Danihelka, Will Dabney, Shakir Mohamed, Balaji Lakshminarayanan, Stephan Hoyer, and Rémi Munos. The cramer distance as a solution to biased Wasserstein gradients. *arXiv preprint arXiv:1705.10743*, 2017.
- [6] Yann Brenier. Polar factorization and monotone rearrangement of vector-valued functions. *Communications on pure and applied mathematics*, 44(4):375–417, 1991.
- [7] Jiezhong Cao, Langyuan Mo, Yifan Zhang, Kui Jia, Chunhua Shen, and Minghui Tan. Multi-marginal Wasserstein GAN. *arXiv preprint arXiv:1911.00888*, 2019.
- [8] Yucheng Chen, Matus Telgarsky, Chao Zhang, Bolton Bailey, Daniel Hsu, and Jian Peng. A gradual, semi-discrete approach to generative network training via explicit Wasserstein minimization. In *International Conference on Machine Learning*, pages 1071–1080. PMLR, 2019.
- [9] Jiaojiao Fan, Amirhossein Taghvaei, and Yongxin Chen. Scalable computations of Wasserstein barycenter via input convex neural networks. *arXiv preprint arXiv:2007.04462*, 2020.
- [10] Werner Fenchel. On conjugate convex functions. *Canadian Journal of Mathematics*, 1(1):73–77, 1949.
- [11] Aude Genevay, Marco Cuturi, Gabriel Peyré, and Francis Bach. Stochastic optimization for large-scale optimal transport. In *Advances in neural information processing systems*, pages 3440–3448, 2016.
- [12] Ishaan Gulrajani, Faruk Ahmed, Martin Arjovsky, Vincent Dumoulin, and Aaron C Courville. Improved training of Wasserstein GANs. In *Advances in Neural Information Processing Systems*, pages 5767–5777, 2017.
- [13] Martin Heusel, Hubert Ramsauer, Thomas Unterthiner, Bernhard Nessler, and Sepp Hochreiter. GANs trained by a two time-scale update rule converge to a local nash equilibrium. In *Advances in neural information processing systems*, pages 6626–6637, 2017.
- [14] Leonid Kantorovitch. On the translocation of masses. *Management Science*, 5(1):1–4, 1958.
- [15] Diederik P Kingma and Jimmy Ba. Adam: A method for stochastic optimization. *arXiv preprint arXiv:1412.6980*, 2014.
- [16] Alexander Korotin, Vage Egiazarian, Arip Asadulaev, Alexander Safin, and Evgeny Burnaev. Wasserstein-2 generative networks. In *International Conference on Learning Representations*, 2021.
- [17] Alexander Korotin, Lingxiao Li, Justin Solomon, and Evgeny Burnaev. Continuous wasserstein-2 barycenter estimation without minimax optimization. In *International Conference on Learning Representations*, 2021.
- [18] Jacob Leygonie, Jennifer She, Amjad Almahairi, Sai Rajeswar, and Aaron Courville. Adversarial computation of optimal transport maps. *arXiv preprint arXiv:1906.09691*, 2019.
- [19] Huidong Liu, Xianfeng Gu, and Dimitris Samaras. Wasserstein GAN with quadratic transport cost. In *Proceedings of the IEEE International Conference on Computer Vision*, pages 4832–4841, 2019.
- [20] Huidong Liu, GU Xianfeng, and Dimitris Samaras. A two-step computation of the exact GAN Wasserstein distance. In *International Conference on Machine Learning*, pages 3159–3168. PMLR, 2018.

- [21] Shu Liu, Shaojun Ma, Yongxin Chen, Hongyuan Zha, and Haomin Zhou. Learning high dimensional Wasserstein geodesics. *arXiv preprint arXiv:2102.02992*, 2021.
- [22] Ziwei Liu, Ping Luo, Xiaogang Wang, and Xiaoou Tang. Deep learning face attributes in the wild. In *Proceedings of International Conference on Computer Vision (ICCV)*, December 2015.
- [23] Guansong Lu, Zhiming Zhou, Jian Shen, Cheng Chen, Weinan Zhang, and Yong Yu. Large-scale optimal transport via adversarial training with cycle-consistency. *arXiv preprint arXiv:2003.06635*, 2020.
- [24] Mario Lucic, Karol Kurach, Marcin Michalski, Sylvain Gelly, and Olivier Bousquet. Are GANs created equal? a large-scale study. In *Advances in neural information processing systems*, pages 700–709, 2018.
- [25] Yun Luo, Si-Yang Zhang, Wei-Long Zheng, and Bao-Liang Lu. WGAN domain adaptation for eeg-based emotion recognition. In *International Conference on Neural Information Processing*, pages 275–286. Springer, 2018.
- [26] Ashok Vardhan Makkuva, Amirhossein Taghvaei, Sewoong Oh, and Jason D Lee. Optimal transport mapping via input convex neural networks. *arXiv preprint arXiv:1908.10962*, 2019.
- [27] Anton Mallasto, Jes Frellsen, Wouter Boomsma, and Aasa Feragen. (q, p)-Wasserstein GANs: Comparing ground metrics for Wasserstein GANs. *arXiv preprint arXiv:1902.03642*, 2019.
- [28] Anton Mallasto, Guido Montúfar, and Augusto Gerolin. How well do WGANs estimate the Wasserstein metric? *arXiv preprint arXiv:1910.03875*, 2019.
- [29] Paul Milgrom and Ilya Segal. Envelope theorems for arbitrary choice sets. *Econometrica*, 70(2):583–601, 2002.
- [30] Quan Hoang Nhan Dam, Trung Le, Tu Dinh Nguyen, Hung Bui, and Dinh Phung. Threeplayer Wasserstein GAN via amortised duality. In *Proc. of the 28th Int. Joint Conf. on Artificial Intelligence (IJCAI)*, 2019.
- [31] Gabriel Peyré, Marco Cuturi, et al. Computational optimal transport. *Foundations and Trends® in Machine Learning*, 11(5-6):355–607, 2019.
- [32] Thomas Pinetz, Daniel Soukup, and Thomas Pock. On the estimation of the Wasserstein distance in generative models. In *German Conference on Pattern Recognition*, pages 156–170. Springer, 2019.
- [33] Maziar Sanjabi, Jimmy Ba, Meisam Razaviyayn, and Jason D Lee. On the convergence and robustness of training GANs with regularized optimal transport. *arXiv preprint arXiv:1802.08249*, 2018.
- [34] Filippo Santambrogio. Optimal transport for applied mathematicians. *Birkäuser, NY*, 55(58-63):94, 2015.
- [35] Jörn Schrieber, Dominic Schuhmacher, and Carsten Gottschlich. Dotmark—a benchmark for discrete optimal transport. *IEEE Access*, 5:271–282, 2016.
- [36] Vivien Seguy, Bharath Bhushan Damodaran, Rémi Flamary, Nicolas Courty, Antoine Rolet, and Mathieu Blondel. Large-scale optimal transport and mapping estimation. *arXiv preprint arXiv:1711.02283*, 2017.
- [37] Jian Shen, Yanru Qu, Weinan Zhang, and Yong Yu. Wasserstein distance guided representation learning for domain adaptation. In *Proceedings of the AAAI Conference on Artificial Intelligence*, volume 32, 2018.
- [38] Jan Stanczuk, Christian Etmann, Lisa Maria Kreusser, and Carola-Bibiane Schonlieb. Wasserstein GANs work because they fail (to approximate the Wasserstein distance). *arXiv preprint arXiv:2103.01678*, 2021.
- [39] Amirhossein Taghvaei and Amin Jalali. 2-Wasserstein approximation via restricted convex potentials with application to improved training for GANs. *arXiv preprint arXiv:1902.07197*, 2019.
- [40] Cédric Villani. *Topics in optimal transportation*. Number 58. American Mathematical Soc., 2003.
- [41] Cédric Villani. *Optimal transport: old and new*, volume 338. Springer Science & Business Media, 2008.

- [42] Jiqing Wu, Zhiwu Huang, Janine Thoma, Dinesh Acharya, and Luc Van Gool. Wasserstein divergence for GANs. In *Proceedings of the European Conference on Computer Vision (ECCV)*, pages 653–668, 2018.
- [43] Yujia Xie, Minshuo Chen, Haoming Jiang, Tuo Zhao, and Hongyuan Zha. On scalable and efficient computation of large scale optimal transport. volume 97 of *Proceedings of Machine Learning Research*, pages 6882–6892, Long Beach, California, USA, 09–15 Jun 2019. PMLR.

A Benchmark Pairs Details

In Appendix A.1 we discuss the details of high-dimensional benchmark pairs. Appendix A.2 is devoted to CelebA 64×64 images benchmark pairs.

A.1 High-dimensional Benchmark Pairs

The benchmark creation example is given in Figure 4. In each dimension we fix random Gaussian mixtures $\mathbb{P}, \mathbb{Q}_1, \mathbb{Q}_2$ (in the code we hard-code the random seeds) and use them to create a benchmark.

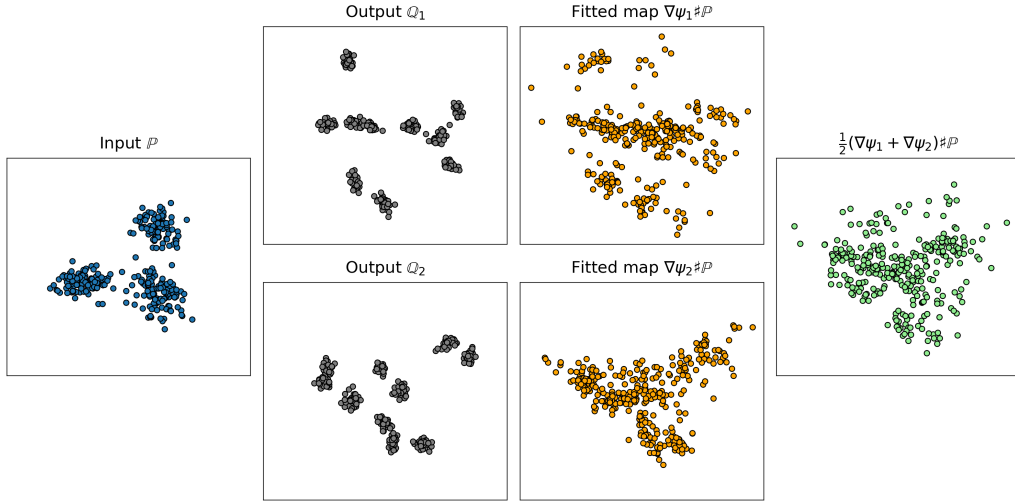


Figure 4: An example of creation of a benchmark pair for dimension $D = 16$. We first initialize 3 random Gaussian Mixtures \mathbb{P} and $\mathbb{Q}_1, \mathbb{Q}_2$ and fit 2 approximate OT maps $\nabla\psi_i\#\mathbb{P} \approx \mathbb{Q}_i, i = 1, 2$. We use the average of potentials to define the output measure: $\frac{1}{2}(\nabla\psi_1 + \nabla\psi_2)\#\mathbb{P}$. Each scatter plot contains 512 random samples projected to 2 principle components of measure $\frac{1}{2}(\nabla\psi_1 + \nabla\psi_2)\#\mathbb{P}$.

To generate a random mixture of M Gaussian measures in dimension D , we use the following procedure. Let $\delta, \sigma > 0$ (we use $\delta = 1, \sigma = \frac{2}{5}$) and consider the M -dimensional grid

$$G = \left\{ -\frac{\delta \cdot M}{2} + i \cdot \delta \text{ for } i = 1, 2, \dots, M \right\}^D \subset \mathbb{R}^D.$$

We pick M random points $\mu'_1, \dots, \mu'_M \in G$ such that no pair of points has any shared coordinate. We initialize random $A'_1, \dots, A'_M \in \mathbb{R}^{D \times D}$, where each row of each matrix is randomly sampled from $D - 1$ dimensional sphere in \mathbb{R}^D . Let $\Sigma'_m = \sigma^2 \cdot (A'_m) \cdot (A'_m)^\top$ for $m = 1, 2, \dots, M$ and note that $[\Sigma'_m]_{dd} = \sigma^2$ for $d = 1, 2, \dots, D$. Next, we consider the Gaussian mixture $\frac{1}{M} \sum_{m=1}^M \mathcal{N}(\mu'_m, \Sigma'_m)$. Finally, we normalize the mixture to have axis-wise variance equal to 1, i.e. we consider the final mixture $\frac{1}{M} \sum_{m=1}^M \mathcal{N}(\mu_m, \Sigma_m)$, where $\mu_m = a\mu'_m$ and $\Sigma_m = a^2\Sigma'_m$. The value $a \in \mathbb{R}_+$ is given by

$$a^{-1} = \sqrt{\frac{\sum_{m=1}^M \|\mu'_m\|^2}{M \cdot D} + \sigma^2}.$$

Gaussian mixtures created by the procedure have D same nice marginals, see Figure 5.

A.2 CelebA 64×64 Images Benchmark Pairs

We fit 3 generative models on CelebA64 aligned faces dataset with a 128-dimensional latent Gaussian measure to sample from their distribution, using WGAN-QC [19] with a ResNet generator network. For trials $k = 1, 2$, we keep generator checkpoints after 1000, 5000, 10000 iterations to produce measures $\mathbb{Q}_{\text{Early}}^k, \mathbb{Q}_{\text{Mid}}^k, \mathbb{Q}_{\text{Late}}^k$ respectively. In the last trial $k = 3$, we keep only the final generator

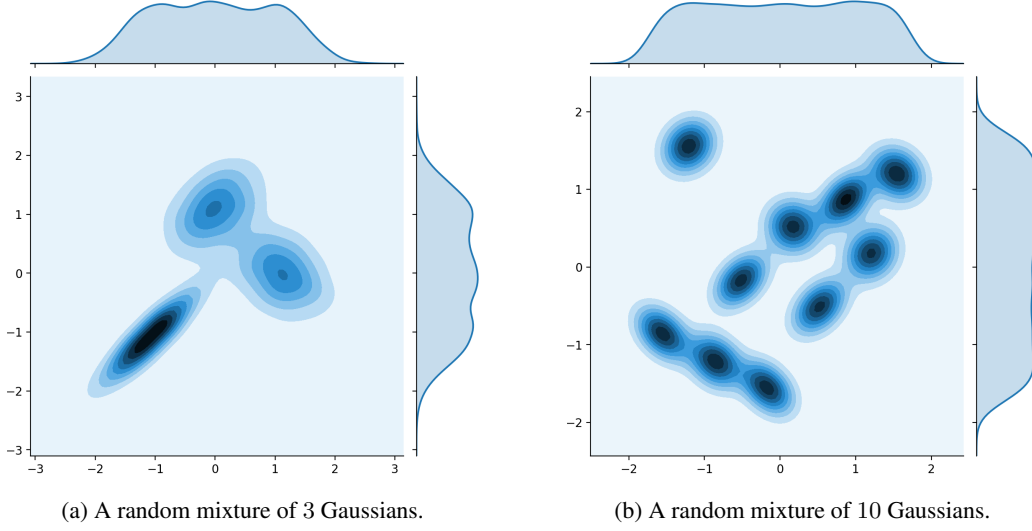


Figure 5: Randomly generated Gaussian mixtures. Projection on to first two dimensions.

network checkpoint after 50000 iterations which produces measure $\mathbb{P}_{\text{Final}}^3$. To make each of measures absolutely continuous, we add white Normal noise (axis-wise $\sigma = 0.01$) to the generators' output.

We use the generated measures to construct images benchmark pairs according to the pipeline described in §4.1. We visualize the pipeline in Figure 6.

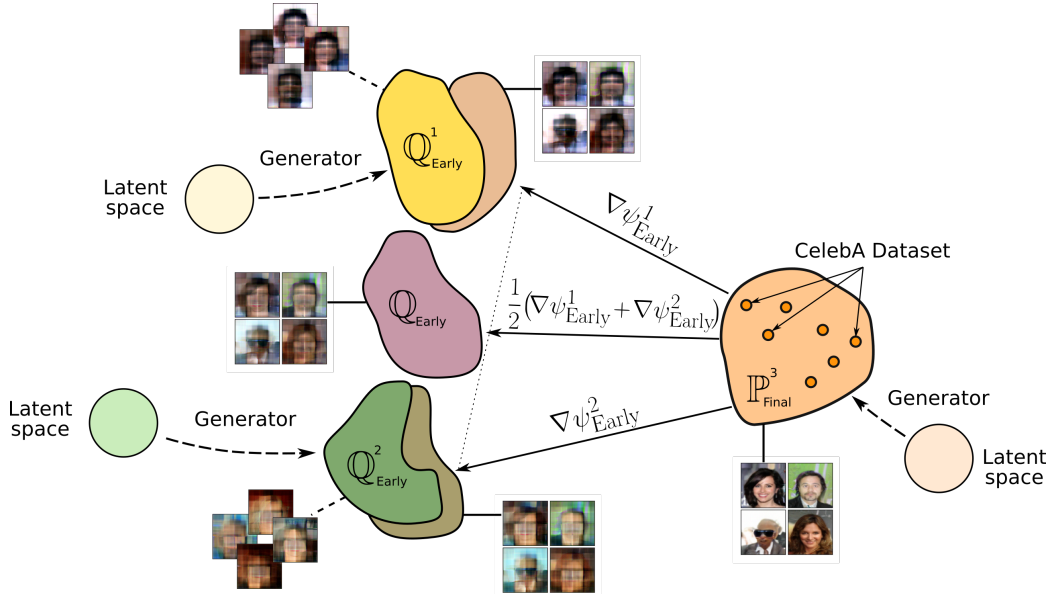


Figure 6: The pipeline of the image benchmark pair creation. We use 3 checkpoints of a generative model: $\mathbb{P}_{\text{Final}}^3$ (well-fitted) and $\mathbb{Q}_{\text{Cpkt}}^1, \mathbb{Q}_{\text{Cpkt}}^2$ (under-fitted). For $k = 1, 2$ we fit an approximate OT map $\mathbb{P}_{\text{Final}}^3 \rightarrow \mathbb{Q}_{\text{Cpkt}}^k$ by $\nabla \psi_{\text{Cpkt}}^k$, i.e. a gradient of ICNN. We define the benchmark pair by $(\mathbb{P}_{\text{CelebA}}, \mathbb{Q}_{\text{Cpkt}}) \stackrel{\text{def}}{=} (\mathbb{P}_{\text{Final}}^3, \frac{1}{2}(\nabla \psi_{\text{Cpkt}}^1 + \nabla \psi_{\text{Cpkt}}^2) \# \mathbb{P}_{\text{Final}}^3)$. In the visualization, Cpkt is Early.

B Experimental Details

In Appendix B.1, we discuss the neural network architectures we used in experiments. All the other training hyperparameters are given in Appendix B.2.

B.1 Neural Network Architectures

In Table 4 below, we list all the neural network architectures we use in continuous OT solvers. In every experiment we pre-train networks to satisfy $\nabla\psi_\theta(x) = x - \nabla f_\theta(x) \approx x$ and $H_\omega(y) \approx y$ at the start of the optimization. We empirically noted that such a strategy leads to more stable optimization.

| Solver | High-dimensional benchmark | CelebA benchmark | CelebA image generation |
|--------------------|--|---|-------------------------|
| [LS] | $\psi_\theta, \phi_\omega : \mathbb{R}^D \rightarrow \mathbb{R}$ - DenseICNN (U) | N/A | |
| [MM-B] | $\psi_\theta : \mathbb{R}^D \rightarrow \mathbb{R}$ - DenseICNN (U) | $f_\theta : \mathbb{R}^D \rightarrow \mathbb{R}$ - ResNet | |
| [QC] | $\psi_\theta : \mathbb{R}^D \rightarrow \mathbb{R}$ - DenseICNN (U) | $f_\theta : \mathbb{R}^D \rightarrow \mathbb{R}$ - ResNet | |
| [MM] | $\psi_\theta : \mathbb{R}^D \rightarrow \mathbb{R}$ - DenseICNN (U) | $f_\theta : \mathbb{R}^D \rightarrow \mathbb{R}$ - ResNet | |
| | $H_\omega : \mathbb{R}^D \rightarrow \mathbb{R}^D$ - ∇ of DenseICNN (U) | $H_\omega : \mathbb{R}^D \rightarrow \mathbb{R}^D$ - UNet | |
| [MM-R] | $T_\theta : \mathbb{R}^D \rightarrow \mathbb{R}^D$ - ∇ of DenseICNN (U) | $T_\theta : \mathbb{R}^D \rightarrow \mathbb{R}^D$ - UNet | |
| | $\phi_\omega : \mathbb{R}^D \rightarrow \mathbb{R}$ - DenseICNN (U) | $g_\omega : \mathbb{R}^D \rightarrow \mathbb{R}$ - ResNet | |
| [MMv1] | $\psi_\theta : \mathbb{R}^D \rightarrow \mathbb{R}$ - DenseICNN | N/A | |
| [MMv2] [W2] | $\psi_\theta : \mathbb{R}^D \rightarrow \mathbb{R}$ - DenseICNN | $\psi_\theta : \mathbb{R}^D \rightarrow \mathbb{R}$ - ConvICNN64 | |
| | $H_\omega : \mathbb{R}^D \rightarrow \mathbb{R}^D$ - ∇ of DenseICNN | $H_\omega : \mathbb{R}^D \rightarrow \mathbb{R}^D$ - ∇ of ConvICNN64 | |
| [MMv2-R] [W2-R] | $T_\theta : \mathbb{R}^D \rightarrow \mathbb{R}^D$ - ∇ of DenseICNN | $T_\theta : \mathbb{R}^D \rightarrow \mathbb{R}^D$ - ∇ of ConvICNN64 | |
| | $\phi_\omega : \mathbb{R}^D \rightarrow \mathbb{R}$ - DenseICNN | $\phi_\omega : \mathbb{R}^D \rightarrow \mathbb{R}$ - ConvICNN64 | |

Table 4: Network architectures we use to parametrize potential f (or ψ) and map H in tested solvers. In the reversed solvers we parametrize second potential g (or ϕ) and forward transport map T by neural networks.

In the **high-dimensional benchmark**, we use DenseICNN architecture from [16, §B.2]. It is a fully-connected neural net with additional input-quadratic skip-connections. This architecture can be made input-convex by limiting certain weights to be non-negative. We impose such as a restriction only for [MMv1],[MMv2],[W2] solvers which require networks to be input-convex. In other cases, the network has no restrictions on weights and we denote the architecture by DenseICNN (U). In experiments, we use the implementation of DenseICNN from the official repository of [W2] solver:

<https://github.com/iamalexkorotin/Wasserstein2GenerativeNetworks>

More precisely, in the experiments with probability measures on \mathbb{R}^D , we use

$$\text{DenseICNN}[1; \max(2D, 64), \max(2D, 64), \max(D, 32)].$$

Here 1 is the rank of the input-quadratic skip connections and the other values define sizes of fully-connected layers the sequential part of the network. The notation follows [16, §B.2].

We emphasize that DenseICNN architecture ψ_θ has differentiable CELU [4] activation functions. Thus, $\nabla\psi_\theta$ is well-defined. In particular, artificial $\beta \cdot \|x\|^2/2$ for $\beta = 10^{-4}$ is added to the output of the last layer of the ICNN. This makes ψ_θ to be β -strongly convex. As the consequence, $\nabla\psi_\theta$ is a bijective function with Lipschitz constant lower bounded by β , see the discussion in [16, §B.1].

In the **experiments with CelebA images**, for parametrizing the potential $f = f_\theta : \mathbb{R}^D \rightarrow \mathbb{R}$ in [MM], [QC], [MM-B], we use ResNet architecture from the official WGAN-QC [19] repository:

<https://github.com/harryliaw/WGAN-QC>

To parametrize the map $H = H_\omega : \mathbb{R}^D \rightarrow \mathbb{R}^D$ in [MM] solver, we use UNet architecture from

<https://github.com/milesial/Pytorch-UNet>

In [MMv2], [W2] solvers we parametrize $\psi = \psi_\theta$ and $H = H_\omega = \nabla\phi_\omega$, where both ψ_θ, ϕ_ω have ConvICNN64 architecture, see Figure 7. We artificially add $\beta \cdot \|x\|^2/2$ (for $\beta = 10^{-4}$) to the output of the output of the ConvICNN64 to make its gradient bijective.

In the architecture, *PosConv2D* layers are usual 2D convolutional layers with all weights (except biases) restricted to be non-negative. *Conv2D-CQ* (convex quadratic) are fully convolutional blocks

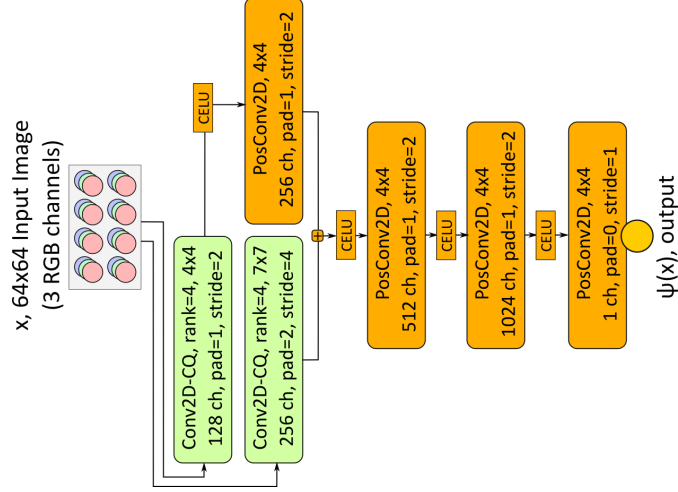


Figure 7: Convolutional ICNN architecture we use for processing 64×64 RGB images.

which output a tensor whose elements are input-quadratic functions of the input tensor. In Figure 8, we present the architecture of Conv2D-CQ block. Here, *GroupChannelSumPool* operation corresponds to splitting the tensor per channel dimension into n_{out} sequential sub-tensors (each of r channels) and collapsing each sub-tensor into one 1-channel tensor by summing r channel maps. The layer can be viewed as the convolutional analog of *ConvexQuadratic* dense layer proposed by [16, §B.2].

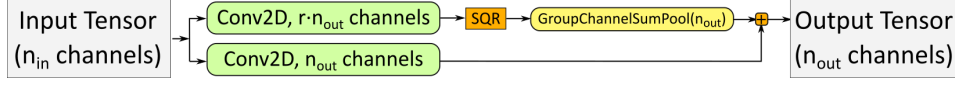


Figure 8: 2D convolutional convex quadratic block.

In the **CelebA image generation experiments**, we also use ResNet architecture for the generator network g . The implementation is taken from WGAN-QC repository mentioned above.

B.2 Hyperparameters and Implementation Details

The evaluation of all the considered continuous solvers for evaluation is not trivial for two reasons. First, not all the solvers have available user-friendly *Python* implementations. Next, some solvers are not used outside the GAN setting. Thus, for considering them in the benchmark, proper extraction of the \mathbb{W}_2 solver (discriminator part) from the GAN is needed.

We implement most of the solvers from scratch. In all the cases, we use Adam optimizer [15] with default hyperparameters (except the learning rate). For solvers [QC] by [19] and [W2] by [16] we use the code provided by the authors in the official papers' GitHub repositories.

B.2.1 High-dimensional Benchmark Pairs

We report the hyper parameters we use in high-dimensional benchmark in Table 5. *Total iterations* column corresponds to optimizing the potential f_θ (or ψ_θ) to *maximize* the dual form (8). In maximin solvers, there is also an inner cycle which corresponds to solving the inner *minimization* problem in (8). The hyperparameters are chosen empirically to best suit the considered evaluation setting.

For [QC] solver large batch sizes are computationally infeasible since it requires solving a linear program at each optimization step [19, §3.1]. Thus, we use batch size 64 as in the original paper. [W2] solver is used with the same hyperparameters in training/evaluation of the benchmarks.

B.2.2 CelebA 64×64 Images Benchmark Pairs

For the images benchmark, we list the hyperparameters in Table 6.

| Solver | Batch Size | Total Iterations | LR | Note |
|-------------|------------|------------------|-----------|---|
| [LS] | 1024 | 100000 | 10^{-3} | Quadratic regularization with $\epsilon = 3 \cdot 10^{-2}$, see [36, Eq. (7)] |
| [MM-B] | 1024 | 100000 | 10^{-3} | None |
| [QC] | 64 | 100000 | 10^{-3} | OT regularization with $K = 1, \gamma = 0.1$, see [19, Eq. (10)] |
| [MMv1] | 1024 | 20000 | 10^{-3} | 1000 gradient iterations ($lr = 0.3$) to compute argmin in (8), see [39, §6]. Early stop when gradient norm $< 10^{-3}$. |
| [MM],[MMv2] | 1024 | 50000 | 10^{-3} | 15 inner cycle iterations to update H_ω , ($K = 15$ in the notation of [26, Algorithm 1]) |
| [W2] | 1024 | 250000 | 10^{-3} | Cycle-consistency regularization, $\lambda = D$, see [16, Algorithm 1] |

Table 5: Hyperparameters of solvers we use in high-dimensional benchmark. Reversed are not presented in this table: they use the same hyperparameters as their original versions.

| Solver | Batch Size | Total Iterations | LR | Note |
|--------|------------|------------------|-------------------|--|
| [MM-B] | 64 | 20000 | $3 \cdot 10^{-4}$ | None |
| [QC] | 64 | 20000 | $3 \cdot 10^{-4}$ | OT regularization with $K = 1, \gamma = 0.1$, see [19, Eq. (10)] |
| [MM] | 64 | 50000 | $3 \cdot 10^{-4}$ | 5 inner cycle iterations to update H_ω , ($K = 5$ in the notation of [26, Algorithm 1]) |
| [W2] | 64 | 50000 | $3 \cdot 10^{-4}$ | Cycle-consistency regularization, $\lambda = 10^4$, see [16, Algorithm 1] |

Table 6: Hyperparameters of solvers we use in CelebA images benchmark.

B.2.3 CelebA 64×64 Images Generation Experiment

To train a generative model, we use GAN-style training: generator network G_α updates are alternating with OT solver’s updates (discriminator’s update). The learning rate for the generator network is $3 \cdot 10^{-4}$ and the total number of generator iterations is 50000.

In [QC] solver we use the code by the authors: there is one gradient update of OT solver per generator update. In all the rest methods, we alternate 1 generator update with 10 updates of OT solver (*iterations* in notation of Table 6). All the rest hyperparameters match the previous experiment.

The generator’s gradient w.r.t. parameters α on a mini-batch $z_1, \dots, z_N \sim \mathbb{S}$ is given by

$$\partial \mathbb{W}_2^2(\mathbb{P}_\alpha, \mathbb{Q}) / \partial \alpha = \int_z \mathbf{J}_\alpha G_\alpha(z)^T \nabla f^*(G_\alpha(z)) d\mathbb{S}(z) \approx \frac{1}{N} \sum_{n=1}^N \mathbf{J}_\alpha G_\alpha(z_n)^T \nabla f_\theta(G_\alpha(z_n)) \quad (10)$$

where \mathbb{S} is the latent space measure and f_θ is the current potential (discriminator) of OT solver. Note that in [MM:R] potential f is not computed but the forward OT map T_θ is parametrized instead. In this case, we estimate the gradient (10) on a mini-batch by $\frac{1}{N} \sum_{n=1}^N \mathbf{J}_\alpha G_\alpha(z_n)^T (\text{id}_{\mathbb{R}^D} - T_\theta)$.